



Deposited via The University of Leeds.

White Rose Research Online URL for this paper:

<https://eprints.whiterose.ac.uk/id/eprint/231027/>

Version: Accepted Version

---

**Article:**

Fayon, A. K., Hansen, L. N., Piazzolo, S. et al. (2025) Dislocation motion enhances Pb mobility in experimentally deformed apatite. *Geology*, 53 (11). pp. 983-987. ISSN: 0091-7613

<https://doi.org/10.1130/G53841.1>

---

This is an author produced version of an article published in *Geology*, made available under the terms of the Creative Commons Attribution License (CC-BY), which permits unrestricted use, distribution and reproduction in any medium, provided the original work is properly cited.

**Reuse**

This article is distributed under the terms of the Creative Commons Attribution (CC BY) licence. This licence allows you to distribute, remix, tweak, and build upon the work, even commercially, as long as you credit the authors for the original work. More information and the full terms of the licence here:

<https://creativecommons.org/licenses/>

**Takedown**

If you consider content in White Rose Research Online to be in breach of UK law, please notify us by emailing [eprints@whiterose.ac.uk](mailto:eprints@whiterose.ac.uk) including the URL of the record and the reason for the withdrawal request.

# 1 Dislocation motion enhances Pb mobility in experimentally 2 deformed apatite

3 **Annia K. Fayon<sup>1</sup>, Lars N. Hansen<sup>1</sup>, Sandra Piazzolo<sup>2</sup>, Amanda Dillman<sup>1</sup> and William O.  
4 Nachlas<sup>3</sup>**

5 <sup>1</sup>*Department of Earth and Environmental Sciences, University of Minnesota-Twin Cities, MN,  
6 55455, USA*

7 <sup>2</sup>*School of Earth and Environment, University of Leeds, LS2 9JT, UK*

8 <sup>3</sup>*Department of Geoscience, University of Wisconsin-Madison, WI, 53706, USA*

## 9 **ABSTRACT**

10 The distribution of Pb in minerals provides a key window into deciphering the timescales of  
11 geologic processes. However, the role of deformation-induced dislocations on Pb mobility and  
12 redistribution remains largely unconstrained. We conducted a series of experiments to constrain the  
13 processes controlling Pb mobility during deformation of apatite. Torsion experiments on single  
14 crystals of Durango apatite at 300 MPa confining pressure and 1100°C resulted in gradual lattice  
15 distortion and a network of subgrain boundaries in response to dislocation nucleation, movement,  
16 and recovery. Results from a static diffusion experiment at the same P-T conditions with a Pb  
17 source are consistent with known rates of volume diffusion. In contrast, torsion of an apatite single  
18 crystal coated in a Pb source revealed substantial mobility of Pb during deformation. This sample  
19 developed similar deformation-related microstructures, containing increased concentrations of Pb in  
20 and near subgrain boundaries. Our results demonstrate that during crystal-plastic deformation of  
21 apatite at these experimental conditions, Pb is transported orders of magnitude farther than  
22 predicted by published diffusivities, highlighting the importance of *active* crystal-plastic  
23 deformation in enhancing Pb mobility in apatite. We suggest that this enhanced mobility results  
24 from the capture and drag of Pb in Cottrell atmospheres associated with mobile dislocations during  
25 crystal-plastic deformation.

26 Our results have important implications for geochronological analyses relying on Pb  
27 concentrations in apatite, which will be affected by deformation below the Pb diffusion closure  
28 temperatures. Similar effects are likely to extend to other trace elements in accessory phases.

## 29 **INTRODUCTION**

30 The distribution of Pb in apatite is commonly used to constrain the timing and rates of a breadth of  
31 geologic processes (e.g., Chew and Spikings, 2021), yet little is known about the mechanisms by  
32 which Pb is mobilized in deformed and/or deforming apatite. Understanding the mechanisms by  
33 which the distribution of Pb in deformed accessory phases is modified is crucial for interpreting  
34 geochronological and thermochronological data (e.g., Engi et al., 2017). Work on engineering  
35 materials has revealed that crystal defects may modify the spatial distribution of trace-elements  
36 (e.g., Cadel et al., 2003), and similar processes have been inferred to occur in accessory minerals. In

37 geological samples, atom-probe tomography analyses demonstrate that trace elements may  
38 preferentially segregate to and accumulate along dislocations in zircon (Piazolo et al., 2016;  
39 Peterman et al., 2016) and rutile (Verberne et al., 2022). The presence and/or activity of  
40 dislocations has been shown to explain apparent age domains in apatite (Odlum et al., 2022),  
41 monazite (e.g., Erickson et al., 2015; Fougrouse et al., 2021a), titanite (Corvò et al., 2023) and  
42 zircon (Reddy et al., 2007; Moser et al., 2009; Timms et al., 2011; Piazolo et al., 2012, 2016). It has  
43 been hypothesized that dislocations may redistribute Pb and affect the distribution of apparent dates  
44 in a mineral by either acting as fast diffusion pathways or by dragging of trace elements (e.g.  
45 zircon: Piazolo et al., 2016; olivine: (Ando et al., 2001); apatite: Odlum et al., 2022, monazite:  
46 (Fougrouse et al., 2021b)a, b). In the first case, fast diffusion pathways remaining after  
47 deformation will continue enhancing Pb mobility. In the second case, Pb mobility will only be  
48 enhanced during deformation. Solute atoms are attracted to dislocations to reduce the overall energy  
49 of the system, forming Cottrell atmospheres. These atmospheres then move with the dislocations  
50 during plastic deformation (Supp). Determining the importance of either mechanism for  
51 redistributing Pb is fundamental to interpreting acquired ages. For example, if active dislocation  
52 movement is necessary for isotopic re-distribution, the apparent age could constrain the timing of  
53 deformation itself (e.g. Piazolo et al. 2012).

54 Here we present a set of deformation and diffusion experiments designed to specifically assess the  
55 influence of either pre-existing (static) or active (dynamic) dislocations on Pb mobility and  
56 therefore the apparent diffusivity of Pb in apatite. We choose apatite because it is widely used to  
57 constrain numerous geologic processes (Chew and Spikings, 2021) and can be easily deformed in  
58 the laboratory.

## 59 **EXPERIMENTAL DESIGN**

60 We conducted three high-pressure (300 MPa), high-temperature (1100°C) experiments on single  
61 crystals of Durango apatite in a Paterson gas-medium apparatus (Paterson and Olgaard, 2000).  
62 Experimental conditions are presented in the Supplementary Material<sup>1</sup>.

63 The null diffusion experiment was conducted to assess the mobility of Pb with no deformation at  
64 the same pressure and temperature as subsequent experiments. The undeformed crystal was coated  
65 in PbZrO<sub>3</sub> (~ 1mm thick) and jacketed in nickel. The sample assembly was held at high PT at  
66 hydrostatic conditions for 5 hours.

67 The static diffusion experiment assessed the mobility of Pb *after* deformation and involved two  
68 steps (Fig. 1A). First, we deformed the single crystal in torsion at high PT to produce a dislocation  
69 microstructure. The crystal was aligned such that the torsion axis was normal to the basal plane and  
70 jacketed as above. Second, the sample was quenched, unjacketed, coated in PbZrO<sub>3</sub>, and rejacketed  
71 for a diffusion experiment identical to our null diffusion experiment.

72 The dynamic diffusion experiment assessed the mobility of Pb *during* deformation. This torsion  
73 experiment was carried out in the same manner as the previous one. However, the sample was  
74 coated with PbZrO<sub>3</sub> powder before being deformed (Fig. 1B).

75 Following experiments, all samples were cut, polished, and analyzed using electron probe  
76 microanalysis (EPMA) for backscatter electron (BSE) imaging and chemical characterization and  
77 electron backscatter diffraction (EBSD) for quantitative orientation analyses (Figs. S1- S3).

## 78 **OBSERVED DEFORMATION AND Pb MOBILITY**

79 The static and dynamic deformation experiments result in distinctly different macroscopic behavior.  
80 Mechanical data from the experiments illustrate that the single crystal is significantly stronger if the  
81 Pb source is present *during* deformation (Fig. 1C). Furthermore, the apatite crystal in the static  
82 experiment exhibits relatively little compositional variation aside from lead zirconate polished into  
83 quench cracks (Fig. 1D), whereas the apatite crystal in the dynamic experiment exhibits  
84 compositionally distinct bands parallel to the basal plane and normal to the torsion axis, as revealed  
85 by elevated BSE signal (i.e., Pb-enrichment; Fig. 1E).

### 86 *Deformation experiments produced significant lattice distortion and subgrain development*

87 EBSD analyses of both deformation experiments reveal that dislocation activity occurred during  
88 deformation (Figs. 2A, B). Deformed samples develop continuous lattice curvature and a network  
89 of subgrain and grain boundaries (Figs. 2A, B). In the static case, high-angle boundaries are  
90 dominant (Fig. 2A), indicating that recovery occurred during the post-deformation diffusion anneal,  
91 whereas in the dynamic experiment the boundaries are primarily low-angle (Fig. 2B).

92 Disorientation axes associated with subgrain boundaries are primarily normal to  $\langle c \rangle$ , which is  
93 consistent with boundaries being composed of edge dislocations gliding in  $\langle a \rangle$  within the basal  
94 plane. This slip system has been inferred to be active in naturally deformed apatite (Odlum et al.,  
95 2022) and was optimally oriented to maximize the resolved shear stress during torsional  
96 deformation. In addition, the general orientation of the crystal (Fig. 2A and B, unit-cell diagrams),  
97 demonstrates that  $\langle c \rangle$  is rotated relative to the starting position normal to the shear plane. This  
98 rotation can be produced by glide of dislocations with Burgers vectors parallel to the  $\langle c \rangle$ ,  
99 consistent with the disorientation axes and observations in natural apatite (Odlum et al., 2022).  
100 Away from the subgrains, lattice curvature of  $\sim 15^\circ$  over  $150 \mu\text{m}$  (Fig. S1) results in a geometrically  
101 necessary dislocation density of  $\sim 10^{13} \text{ m}^{-2}$ , assuming a Burgers vector of 1 nm for  $\langle a \rangle$ .

### 102 *Pb mobility is only enhanced during crystal plastic deformation*

103 A critical relationship is apparent in the dynamic experiment between the bands of subgrains and  
104 the bands of Pb enrichment, which is lacking in the static experiment. High-resolution BSE imaging  
105 of the static experiment confirms the absence of detectable Pb along subgrain bands (Fig. 2C), and  
106 EPMA confirms no measurable Pb within its crystal lattice or subgrain boundaries (Fig. 2E, S2). In  
107 contrast, the dynamic diffusion experiment exhibits a demonstrably higher BSE signal (Fig. 2D)  
108 collocated with subgrain bands (Fig. 2B). EPMA analysis reveals that this elevated BSE signal  
109 corresponds to elevated Pb concentrations (Fig. 2F). These elevated Pb concentrations are not  
110 associated with decompression (quench) cracks formed at the end of the experiment (cf. Fig. 1E) or  
111 contamination from the Pb source during polishing (cf. Fig. 1D). Additional EPMA maps reveal  
112 that these Pb concentrations are associated with Ca depletion (Figs. S2). In summary, Pb is  
113 transported 200 to  $500 \mu\text{m}$  into the sample interior through the apatite lattice along bands of  
114 substructure development *if and only if* deformation is ongoing.

## 115 DISCUSSION AND CONCLUSIONS

### 116 *Dislocation motion is necessary to increase apparent Pb diffusivity in apatite*

117 Our experiments document that Pb mobility in apatite is enhanced *during* crystal-plastic  
118 deformation. As evidenced by both the null and static experiments, in which no Pb infiltration is  
119 observed, static dislocations, subgrain boundaries, and grain boundaries do not produce a  
120 measurable increase in Pb mobility beyond simple lattice diffusion (Fig 2). This observation is  
121 consistent with lattice diffusion estimates based on known diffusivities of Pb in apatite ( $3.6 \times 10^{-13}$   
122  $\text{cm}^2/\text{s}$ ; (Cherniak et al., 1991), which predict a characteristic lattice diffusion length at our  
123 experimental conditions of  $\sim 1 \mu\text{m}$ . Alternatively, fast-path diffusion along dislocations could be as  
124 much as 3 to 4 orders of magnitude faster (e.g., Hirth and Kohlstedt, 2015). However, even with a  
125 pipe diffusivity of  $3.6 \times 10^{-9} \text{cm}^2/\text{s}$ , the apparent bulk diffusivity is expected to increase by only  
126  $\sim 30\%$  (assuming distributed dislocations, a dislocation core radius of twice the Burgers vector  
127 magnitude, and a dislocation density of  $10^{13} \text{m}^{-2}$ ). In the most extreme case of only looking at  
128 diffusion *within* the subgrain boundaries, the characteristic diffusion length is still only 10s of  $\mu\text{m}$   
129 (assuming the boundaries have a similar diffusivity to pipe diffusion and a dislocation density of  
130  $10^{14} \text{m}^{-2}$ , corresponding to a misorientation of  $\sim 10^\circ$ ). In summary, neither lattice nor fast-path  
131 diffusion of Pb can explain the apparent 100–500  $\mu\text{m}$  of Pb transport observed in the dynamic  
132 experiment.

133 Alternatively, we argue that Pb is captured in and around dislocation cores in Cottrell atmospheres  
134 (Supp) and is dragged into the sample interior by mobile dislocations. This segregation and  
135 dragging is a well-known phenomenon in metals (e.g., Cottrell and Bilby, 1949; Blavette et al.,  
136 1999; Cadel et al., 2003), and importantly, the dragging of Cottrell atmospheres by dislocations  
137 may result in macroscopic hardening of the material (Takeuchi and Argon, 1976). Segregation is  
138 evidenced in our experiments by high Pb concentrations in regions of high dislocation density.  
139 Dragging is evidenced in our experiments by increased shear strength in the dynamic experiment  
140 relative to the static experiment (Fig. 1C). Segregation of trace elements to Cottrell atmospheres has  
141 also been observed in some natural settings, including in zircon (Piazolo et al., 2016), rutile  
142 (Verberne et al., 2022), monazite (Fougerouse et al., 2021), and xenotime (Joseph et al., 2024).

143 Our interpretation that enhanced Pb mobility in our dynamic experiment results from dislocation  
144 related Pb capture and dragging requires that dislocations move from the exterior to the interior of  
145 the sample in these experiments. This requirement is consistent with the inferred primary active slip  
146 system (slip on the basal plane in  $\langle a \rangle$ ) in combination with the geometry of torsional deformation  
147 (Fig. 3A). We suggest that dislocation loops nucleate at the outer edge of the sample where stresses  
148 and strain rates are highest, and as the loops expand, the captured Pb is dragged inwards from the  
149 sample exterior (Fig. 3B). None of the Zr, which was also contained in the Pb source, is observed in  
150 the grain interior (Fig. S3) suggesting a preferential capture of Pb. The correlation between high Pb  
151 and low Ca concentrations in EPMA maps suggests that Pb is substituting for Ca in the lattice (Fig.  
152 S2). Furthermore, we argue Pb continues to concentrate along subgrain boundaries as dislocations  
153 organize during syn-deformation recovery (Figs. 2, 3B-D).

### 154 *Implications for U-Pb dates in deformed apatite*

155 The experiments presented here were conducted in the absence of fluids and demonstrate that  
156 dislocations can drag Pb, in what we interpret to be Cottrell atmospheres, through an apatite crystal

157 during deformation. This process produces heterogenous Pb distributions within a deforming grain  
158 as dislocations migrate, accumulate, and arrange into subgrain boundaries, resulting in apparent  
159 orders of magnitude faster transport than other diffusion mechanisms. In our experiments, the  
160 torsional geometry dictates that dislocations primarily move from the edge of the sample inwards.  
161 However, in nature, we envision that Pb primarily migrates with dislocations toward grain  
162 boundaries, effectively removing Pb from the grain. The enhanced mobility of Pb during  
163 deformation can skew thermochronometric dates obtained from U-Pb dating of apatite and  
164 potentially other accessory minerals that record crystal-plastic deformation (Piazolo et al., 2012;  
165 Moser et al., 2022). It is important to note that apatite can record crystal-plastic deformation below  
166 the closure temperature for Pb.

167 To assess the impact of our results on the interpretation of thermochronometric data, we consider  
168 the effect of timing of deformation on apatite grains in the absence of fluids after they have cooled  
169 below the closure temperature ( $T_c$ ) for Pb. During crystal-plastic deformation, mobile dislocations  
170 will work to remove Pb from the crystal interiors, potentially in a heterogeneous manner that  
171 removes more Pb in some regions than others. This heterogeneous Pb mobilization will produce  
172 regions of apparently younger dates. If deformation occurs soon after the grain has cooled below  $T_c$   
173 then the subsequent accumulation of radiogenic Pb over time will obscure the age domains. If,  
174 however, deformation occurs after a significant amount of radiogenic Pb has accumulated, the  
175 heterogeneity of age domains will be greater and more observable. The younger age domains would  
176 be related to the timing of deformation. This scenario is similar to what has been observed in  
177 natural apatite (Odlum et al. 2022) and titanite (Moser et al. 2022; Corvo et al., 2023; [Langone et al.](#)  
178 [2025](#)).

179 Here we highlight the implications of increased Pb mobility from the presence and activation of  
180 dislocations in apatite. Atom-probe tomography on other naturally deformed accessory phases has  
181 documented the increased concentration of other trace elements in these defects (Peterman et al.,  
182 2016; Verberne et al., 2022). Higher observed concentrations are consistent with movement of trace  
183 elements towards dislocations, consistent with fast-path diffusion and document the importance of  
184 this mechanism over geologic timescales. Here we show that another important mechanism, drag by  
185 dislocations *during* deformation, can significantly alter the distribution of a trace element in a  
186 deformed accessory phase, highlighting the need to assess the presence and nature of the  
187 deformation of the studied grains. Although we explicitly use apatite and U-Pb in these  
188 experiments, this process could be relevant to any mineral that experiences deformation enhanced  
189 mobility of trace elements and/or a daughter element.

## 190 **ACKNOWLEDGEMENTS**

191 Thoughtful reviews by A. Ault, M. Odlum, D. Fougereuse and D. Chew greatly improved this  
192 contribution. We also acknowledge insightful discussion about this work with D. Kohlstedt, M.  
193 Zimmerman, J. Mitchell, and H. Wiesman. Fayon was supported by NSF-EAR award 1727203.  
194 Parts of this work were carried out in the Characterization Facility, University of Minnesota, which  
195 receives partial support from the NSF through the MRSEC (Award Number DMR-2011401) and  
196 the NNCI (Award Number ECCS-2025124) programs. SP and LH acknowledge the Cheney  
197 Fellowship (2021-2025) awarded to LH.

198 **FIGURE CAPTIONS**

199 *Figure 1:* A and B) Schematic of sample assemblies. dashed box in A and B indicate location of D  
200 and E. C) Mechanical data for both deformation experiments. D and E) Sample-scale BSE images  
201 of both deformation experiments cut perpendicular to the basal plane. White dashed box in E  
202 indicate locations of Figure 2B, D, and F.

203 *Figure 2:* A and B) EBSD maps of substructure in static and dynamic diffusion experiments. Maps  
204 are colored by disorientation to a reference point, for which the orientation is shown by unit-cell  
205 diagrams. Grain boundaries (disorientations  $>10^\circ$ ) and subgrain boundaries (disorientations of 2-  
206  $10^\circ$ ) indicated by black and gray lines, respectively. C and D) BSE images of regions in A and B.  
207 White dashed box indicates location of map in B. E and F) Qualitative EMP maps of Pb  
208 concentration in the same regions as C and D.

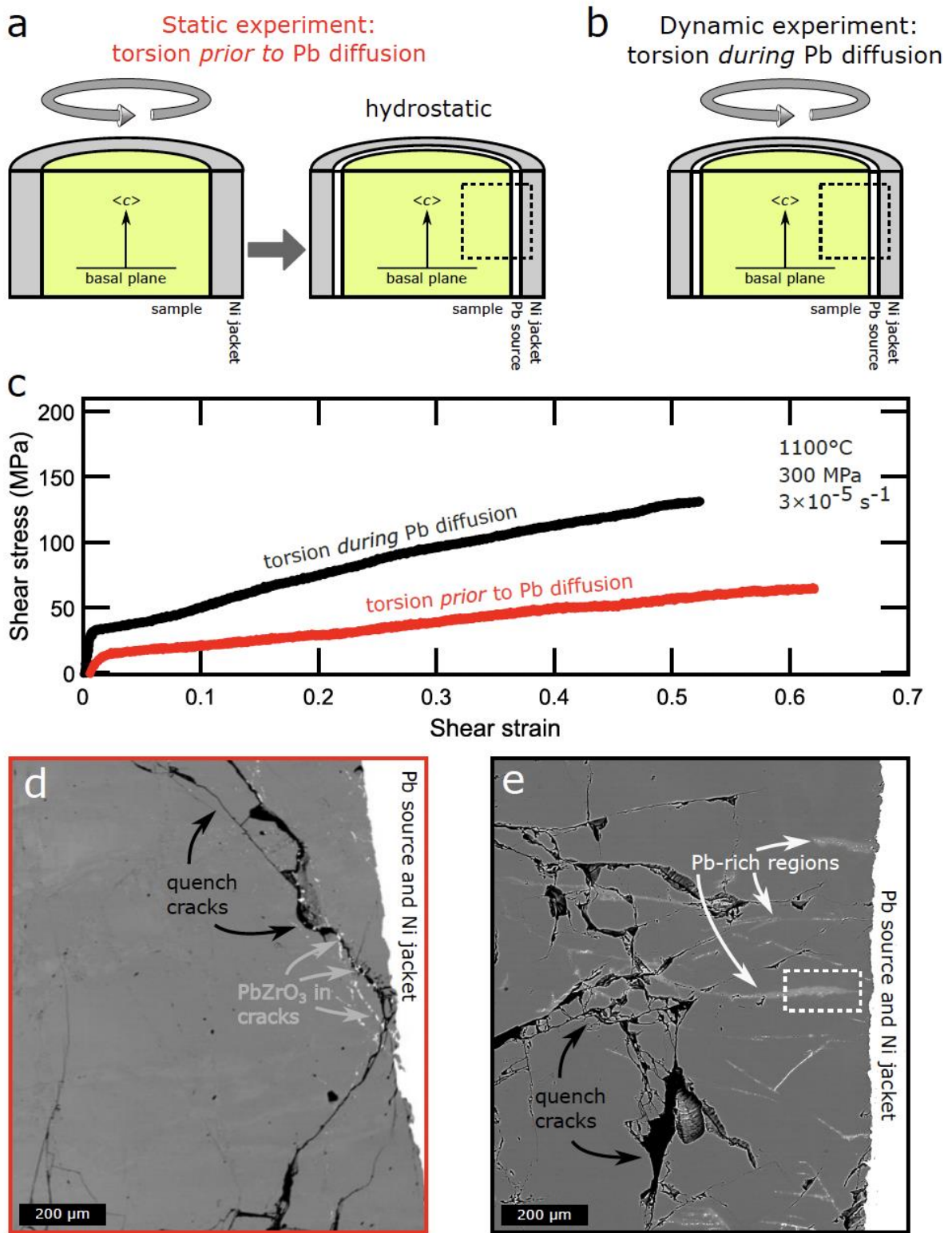
209 *Figure 3.* A) Schematic representation of slip in the apatite sample. Pb is drawn into the crystal by  
210 dislocation loops expanding into the sample interior. B-D) Progression of Pb entrained by  
211 dislocations at the edge of the sample. With increasing strain, dislocations organize into subgrain  
212 boundaries resulting in higher concentrations of Pb along those boundaries.

213 **REFERENCES**

- 214 Ando, J., Shibata, Y., Okajima, Y., Kanagawa, K., Furusho, M., and Tomioka, N., 2001, Striped  
215 iron zoning of olivine induced by dislocation creep in deformed peridotites: *Nature*, v. 414, p.  
216 893–895.
- 217 Blavette, D., Cadel, E., Fraczkiewicz, A., and Menand, A., 1999, Three-dimensional atomic-scale  
218 imaging of impurity segregation to line defects: *Science*, v. 286, p. 2317–2319.
- 219 Cadel, E., Fraczkiewicz, A., and Blavette, D., 2003, Atomic Scale Investigation of Impurity  
220 Segregation to Crystal Defects: *Annual review of materials research*, v. 33, p. 215–231.
- 221 Cherniak, D.J., Lanford, W.A., and Ryerson, F.J., 1991, Lead diffusion in apatite and zircon using  
222 ion implantation and Rutherford Backscattering techniques: *Geochimica et cosmochimica acta*,  
223 v. 55, p. 1663–1673.
- 224 Chew, D.M., and Spikings, R.A., 2021, Apatite U-Pb thermochronology: A review: *Minerals*  
225 (Basel, Switzerland), v. 11, p. 1095.
- 226 Corvò, S., Maino, M., Piazzolo, S., Kylander-Clark, A.R.C., Orlando, A., Seno, S., and Langone, A.,  
227 2023, Crystal plasticity and fluid availability govern the ability of titanite to record the age of  
228 deformation: *Earth and planetary science letters*, v. 620, p. 118349.
- 229 Cottrell, A.H., and Bilby, B.A., 1949, Dislocation Theory of Yielding and Strain Ageing of Iron:  
230 *Proceedings of the Physical Society. Section A*, v. 62, p. 49.
- 231 Engi, M., Lanari, P., and Kohn, M.J., 2017, 1. Significant ages - an introduction to petrochronology,  
232 *in* Kohn, M.J., Engi, M., and Lanari, P. eds., *Petrochronology*, Berlin, Boston, De Gruyter, p.  
233 1–12.
- 234 Erickson, T.M., Pearce, M.A., Taylor, R.J.M., Timms, N.E., Clark, C., Reddy, S.M., and Buick,  
235 I.S., 2015, Deformed monazite yields high-temperature tectonic ages: *Geology*, v. 43, p. 383–  
236 386.

- 237 Fougrouse, D., Cavosie, A.J., Erickson, T., Reddy, S.M., Cox, M.A., Saxey, D.W., Rickard,  
238 W.D.A., and Wingate, M.T.D., 2021a, A new method for dating impact events – Thermal  
239 dependency on nanoscale Pb mobility in monazite shock twins: *Geochimica et cosmochimica*  
240 *acta*, v. 314, p. 381–396.
- 241 Fougrouse, D., Reddy, S.M., Seydoux-Guillaume, A.-M., Kirkland, C.L., Erickson, T.M., Saxey,  
242 D.W., Rickard, W.D.A., Jacob, D., Leroux, H., and Clark, C., 2021b, Mechanical twinning of  
243 monazite expels radiogenic lead: *Geology*, v. 49, p. 417–421.
- 244 Hirth, G., and Kohlstedt, D.L., 2015, The stress dependence of olivine creep rate: Implications for  
245 extrapolation of lab data and interpretation of recrystallized grain size: *Earth and planetary*  
246 *science letters*, v. 418, p. 20–26.
- 247 Joseph, C., Fougrouse, D., Cavosie, A.J., Olierook, H.K.H., Reddy, S.M., Tacchetto, T., Quintero,  
248 R.R., Kennedy, A., Saxey, D.W., and Rickard, W.D.A., 2024, Towards a new impact  
249 geochronometer: Deformation microstructures and U-Pb systematics of shocked xenotime:  
250 *Geochimica et cosmochimica acta*, v. 374, p. 33–50.
- 251 Langone, A., Simonetti, M., Corvò, S., Bonazzi, M., Maino, M., Orlando, A., Braschi, E. and  
252 Piazzolo, S., 2025. Reactive and resilient: the contrasting behaviour of monazite and titanite  
253 during deformation (the Forno-Rosarolo shear zone; Ivrea-Verbanò Zone): *Geological*  
254 *Magazine*, 162, p.e18.
- 255 Moser, D.E., Davis, W.J., Reddy, S.M., Flemming, R.L., and Hart, R.J., 2009, Zircon U–Pb strain  
256 chronometry reveals deep impact-triggered flow: *Earth and planetary science letters*, v. 277, p.  
257 73–79.
- 258 Moser, A.C., Hacker, B.R., Gehrels, G.E., Seward, G.G.E., Kylander-Clark, A.R.C., and Garber,  
259 J.M., 2022, Linking titanite U–Pb dates to coupled deformation and dissolution–  
260 reprecipitation: Contributions to mineralogy and petrology. *Beitrage zur Mineralogie und*  
261 *Petrologie*, v. 177, doi:10.1007/s00410-022-01906-9.
- 262 Odlum, M.L., Levy, D.A., Stockli, D.F., Stockli, L.D., and DesOrmeau, J.W., 2022, Deformation  
263 and metasomatism recorded by single-grain apatite petrochronology: *Geology*, v. 50, p. 697–  
264 703.
- 265 Paterson, M.S., and Olgaard, D.L., 2000, Rock deformation tests to large shear strains in torsion:  
266 *Journal of Structural Geology*, v. 22, p. 1341–1358.
- 267 Peterman, E.M., Reddy, S.M., Saxey, D.W., Snoeyenbos, D.R., Rickard, W.D.A., Fougrouse, D.,  
268 and Kylander-Clark, A.R.C., 2016, Nanogeochronology of discordant zircon measured by atom  
269 probe microscopy of Pb-enriched dislocation loops: *Science advances*, v. 2, p. e1601318.
- 270 Piazzolo, S., Austrheim, H., and Whitehouse, M., 2012, Brittle-ductile microfabrics in naturally  
271 deformed zircon: Deformation mechanisms and consequences for U-Pb dating: *The American*  
272 *mineralogist*, v. 97, p. 1544–1563.
- 273 Piazzolo, S., La Fontaine, A., Trimby, P., Harley, S., Yang, L., Armstrong, R., and Cairney, J.M.,  
274 2016, Deformation-induced trace element redistribution in zircon revealed using atom probe  
275 tomography: *Nature communications*, v. 7, p. 10490.
- 276 Reddy, S.M., Timms, N.E., Pantleon, W., and Trimby, P., 2007, Quantitative characterization of  
277 plastic deformation of zircon and geological implications: Contributions to mineralogy and  
278 petrology. *Beitrage zur Mineralogie und Petrologie*, v. 153, p. 625–645.

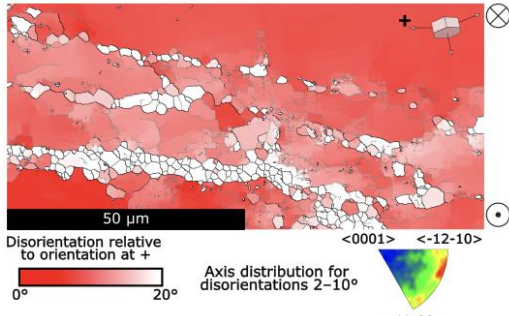
- 279 Takeuchi, S., and Argon, A., 1976, Steady-state creep of alloys due to viscous motion of  
280 dislocations☆: *Acta Metallurgica*, v. 24, p. 883–889.
- 281 Timms, N.E., Kinny, P.D., Reddy, S.M., Evans, K., Clark, C., and Healy, D., 2011, Relationship  
282 among titanium, rare earth elements, U–Pb ages and deformation microstructures in zircon:  
283 Implications for Ti-in-zircon thermometry: *Chemical geology*, v. 280, p. 33–46.
- 284 Verberne, R., Reddy, S.M., Saxey, D.W., Fougereuse, D., Rickard, W.D.A., Quadir, Z., Evans,  
285 N.J., and Clark, C., 2022, Dislocations in minerals: Fast-diffusion pathways or trace-element  
286 traps? *Earth and planetary science letters*, v. 584, p. 117517.
- 287 <sup>1</sup>Supplemental Material. [Details of deformation experiments, scanning electron microscopy, and  
288 electron microprobe analyses] Please visit <https://doi.org/10.1130/XXXX> to access the  
289 supplemental material, and contact [editing@geosociety.org](mailto:editing@geosociety.org) with any questions.
- 290



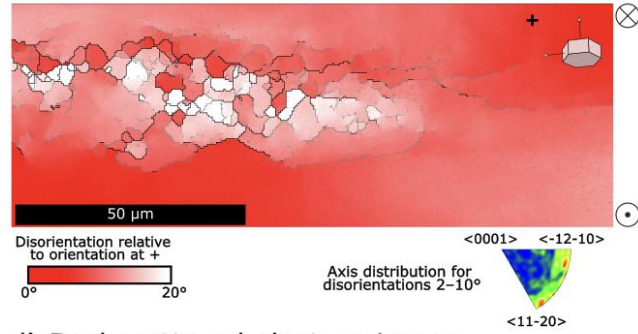
Torsion *prior to*  
Pb-diffusion experiment

Torsion *during*  
Pb-diffusion experiment

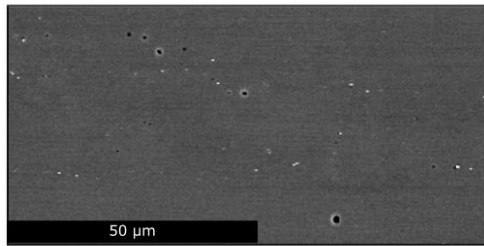
a) EBSD orientation map



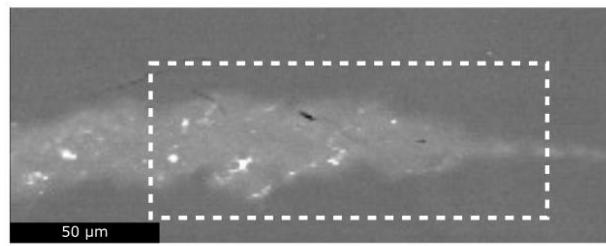
b) EBSD orientation map



c) Backscattered electron image



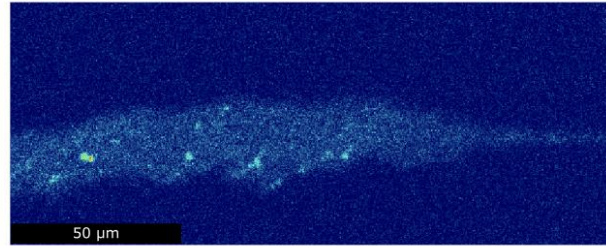
d) Backscattered electron image



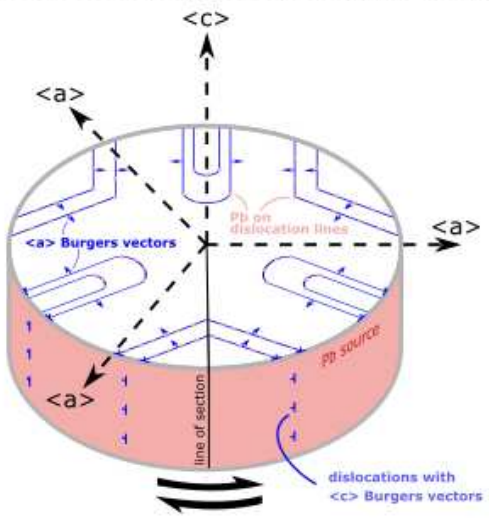
e) Qualitative Pb-intensity EMP map



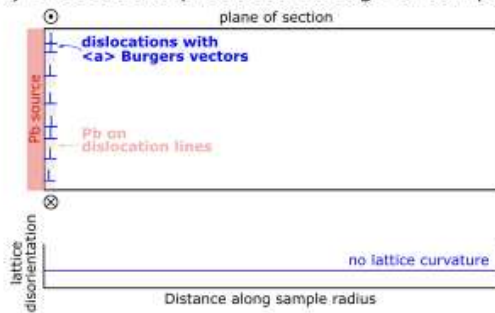
f) Qualitative Pb-intensity EMP map



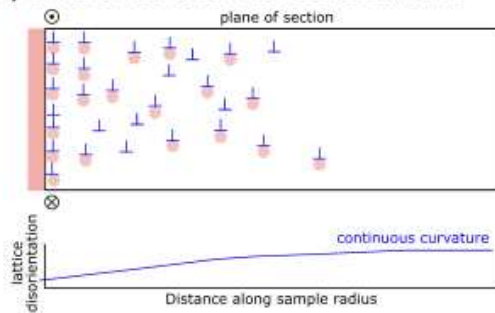
a) Apatite sample with dislocation lines and Burgers vectors relative to crystallographic axes



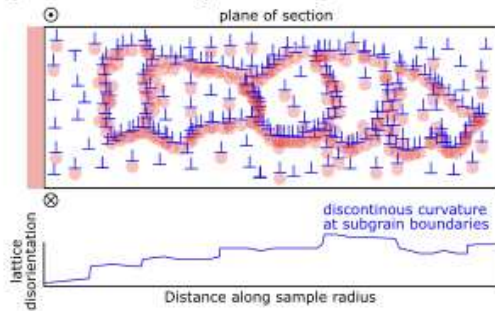
b) Dislocations produced at edge of sample



c) Inward motion of dislocations and Pb



d) Partial recovery and subgrain formation



Increasing time and strain

## 301 SUPPLEMENTAL MATERIALS

### 302 *Section A: A brief note on Cottrell Atmospheres*

303 Segregation and dragging of impurities by dislocations is a well-known phenomenon in metals and ceramics  
304 (e.g., Cottrell and Bilby, 1949; Blavette et al., 1999; Cadel et al., 2003). Distortion of the crystal lattice  
305 around a dislocation results in local lattice sites that are more energetically favorable for impurity atoms than  
306 pristine lattice. This energetic benefit drives segregation of impurities from the surrounding area to the  
307 distorted areas near dislocations. The regions around dislocations into which impurities are segregated are  
308 referred to as Cottrell atmospheres (Cottrell and Bilby, 1949). In theory, these atmospheres can form at any  
309 temperature due to the driving force from the presence of dislocations, and the rate at which they form is  
310 dependent on a number of variables including temperature, stress, strain rate, and dislocation density. The  
311 rate of segregation of the impurities is controlled by their lattice diffusivity. At higher temperatures, the  
312 lattice diffusivity is higher, which will in turn enhance the rate at which the atmosphere forms. Once the  
313 atmosphere forms around a dislocation, it will move through the crystal with the defect. A Cottrell  
314 atmosphere around a dislocation results in a hardening or strengthening of the material, as it becomes more  
315 difficult for the dislocation to move through the lattice with the atmosphere in tow (c.f Fig. 1C). If the  
316 applied stress is high enough, a dislocation can break free of the Cottrell atmosphere, leaving a region with  
317 higher concentrations of impurities.

### 318 *Section B: High-temperature, high-pressure deformation experiments*

319 Apatite single crystals were cut into wafers approximately 3 mm thick ranging between 7 and 9 mm in  
320 diameter. Wafers were orientated with  $\langle c \rangle$  parallel to the cylindrical axis of the sample. In each experiment,  
321 apatite samples were placed between porous alumina spacers and first jacketed in Ni and then in Fe. In some  
322 experiments, the sample was initially coated with  $\text{PbZrO}_3$  powder around the outer circumference prior to  
323 being jacketed. The  $\text{PbZrO}_3$  compound was chosen as a Pb source due to its refractory nature.

324 Completed sample assemblies were then inserted into a Paterson gas-medium apparatus (Paterson and  
325 Olgaard, 2000). The vessel was pressurized to 300 MPa using argon as the pressure medium, and the sample  
326 was heated to 1100°C with a furnace internal to the pressure vessel. For each experiment, the sample was  
327 held at the target conditions for 5 hours.

328 In our null experiment, the crystal was coated in  $\text{PbZrO}_3$  and then brought to target conditions with no  
329 deformation applied at any stage. In our static-diffusion experiment, the crystal was brought to target  
330 conditions and then deformed in torsion for 5 hours. The sample was quenched, removed from the assembly,  
331 coated with  $\text{PbZrO}_3$ , re-jacketed, and brought back to target conditions for an additional 5 hours with no  
332 further deformation. In our dynamic-diffusion experiment, the crystal was initially coated in  $\text{PbZrO}_3$ , brought  
333 to target conditions, and then deformed in torsion for 5 hours.

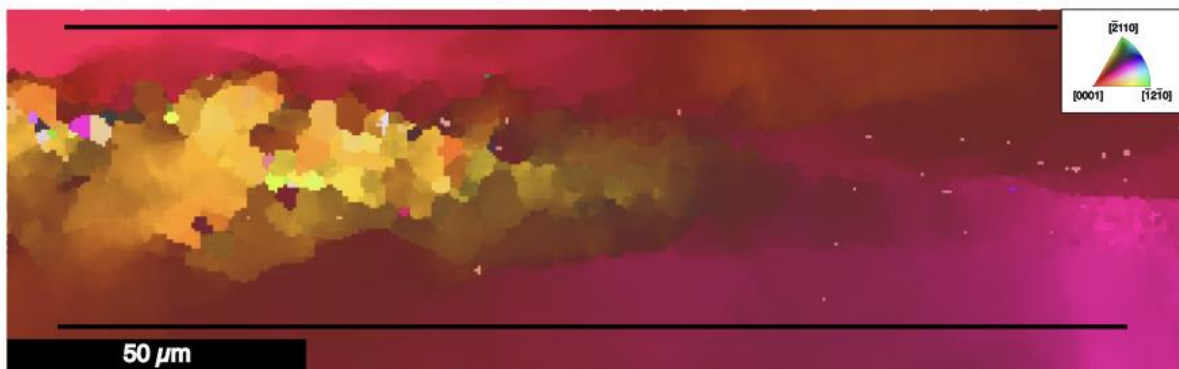
334 In experiments involving torsional deformation, a constant twist rate was applied. This twist rate was set  
335 based on the sample dimensions such that the shear strain rate at the outer radius was  $3 \times 10^{-5} \text{ s}^{-1}$ . The torque  
336 necessary to maintain that rate was recorded throughout the experiment. Torque data were corrected for the  
337 strength of the jacket material using published flow laws for Ni and Fe (Frost and Ashby, 1982). Torque data  
338 were then converted to shear stress at the outer radius following the procedure outlined by Paterson and  
339 Olgaard (2000) with a stress exponent of 2, which has been previously measured in compression experiments  
340 on single crystals of apatite (Fayon and Hansen, 2018). Shear stresses throughout each deformation  
341 experiment are presented in Fig. 1c. Both experiments exhibited significant strain hardening. There is a  
342 notable increase in strength for the sample coated in  $\text{PbZrO}_3$  before deformation.

343 *Section C: Electron backscatter diffraction analysis (EBSD)*

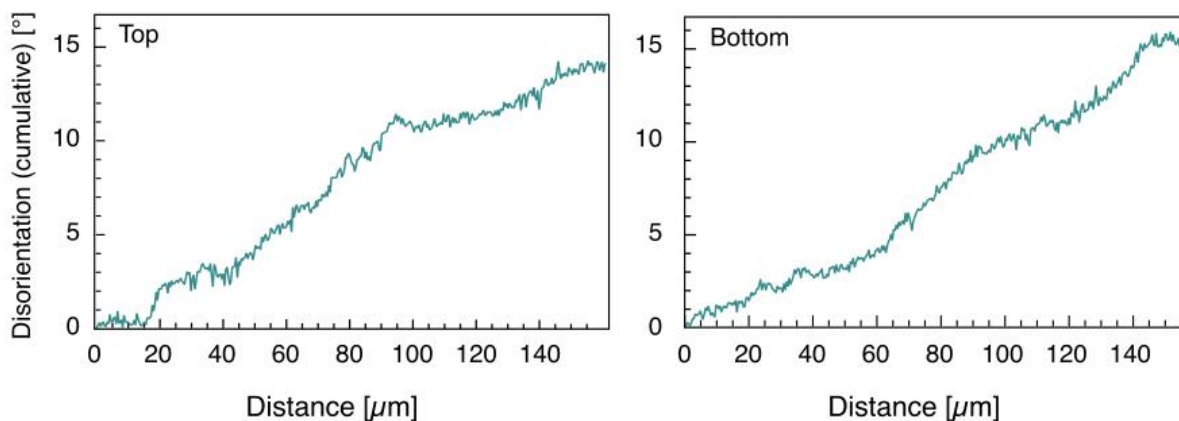
344 Longitudinal sections of the deformed apatite crystals were cut and polished with diamond suspensions of  
345 decreasing size down to 0.05  $\mu\text{m}$ . Samples were subsequently analyzed in a Thermo Apreo 2S Lo-Vac  
346 scanning electron microscope in the Characterization Facility at the University of Minnesota. Data were  
347 acquired using a beam current of 26 nA, an accelerating voltage of 20 kV, a working distance of 15 mm, and  
348 a stage tilt of 70°. An Oxford Instruments Symmetry detector for electron backscatter diffraction was used to  
349 collect maps of crystal orientation with a 0.2  $\mu\text{m}$  step size.

350 Subsequent to mapping, EBSD data were processed using the Oxford Instruments AZtec Crystal software  
351 package. The processing routine consisted of removing wild spikes, interpolating orientations for missing  
352 pixels based on five nearest neighbors, and finally correcting for systematic misindexing of apatite by 60°  
353 around  $\langle c \rangle$ . In construction of maps and inverse pole figures, grain boundaries were defined as  
354 misorientations between neighboring pixels of  $>10^\circ$  and subgrain boundaries were defined as misorientations  
355 of 2 to  $10^\circ$ . Data used to calculate geometrically necessary dislocation density using equation 13 from REF  
356 are shown in Fig. S1.

a) Inverse Pole Figure map



b) line scans



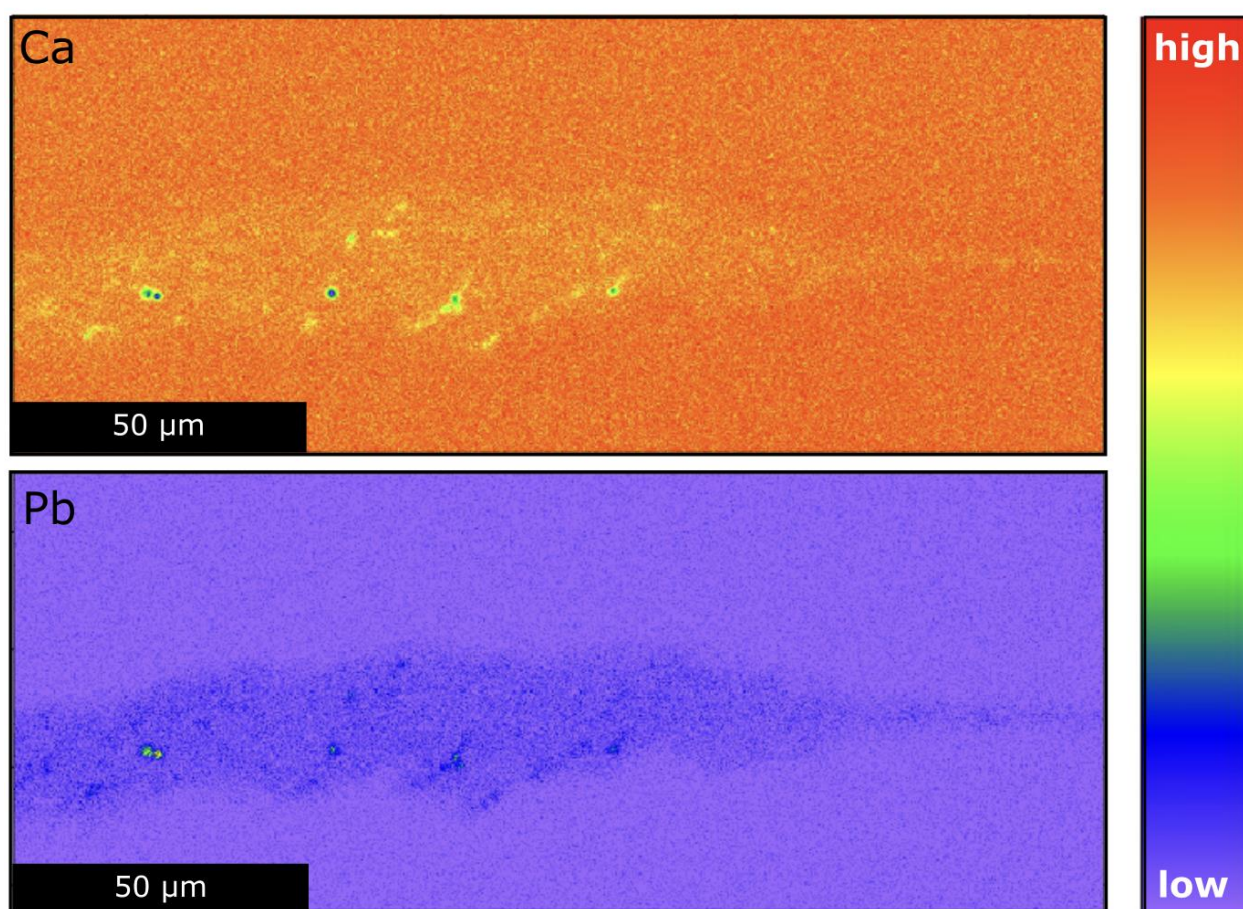
357

358 Figure S1. Radial transects across dynamic deformation experiment. A. Inverse pole figure map is shown  
359 relative to the vertical axis. Black lines indicate locations of line scans shown in B. Data document a lattice  
360 curvature of  $\sim 15^\circ$  over  $\sim 150 \mu\text{m}$ , corresponding to a geometrically necessary dislocation density of  $\sim 10^{13} \text{m}^{-2}$   
361 .

362 *Electron microprobe analysis (EPMA)*

363 Backscatter electron (BSE) images and qualitative element data were collected using a JEOL JXA-  
364 8530FPlus Electron Probe Microanalyzer (EPMA) (Fig. S2) in the Characterization Facility at the University  
365 of Minnesota. BSE images were collected with an accelerating voltage of 15kV and probe current of 15 nA.  
366 The qualitative element maps for Pb and Ca were collected using a probe current of 200 nA. Peaks were  
367 identified using Pb metal and Durango apatite. According to the factory documentation, the Pb  
368 detection limit for this microanalyzer is 30 ppm. Note the actual detection limits depend on  
369 analytical conditions.

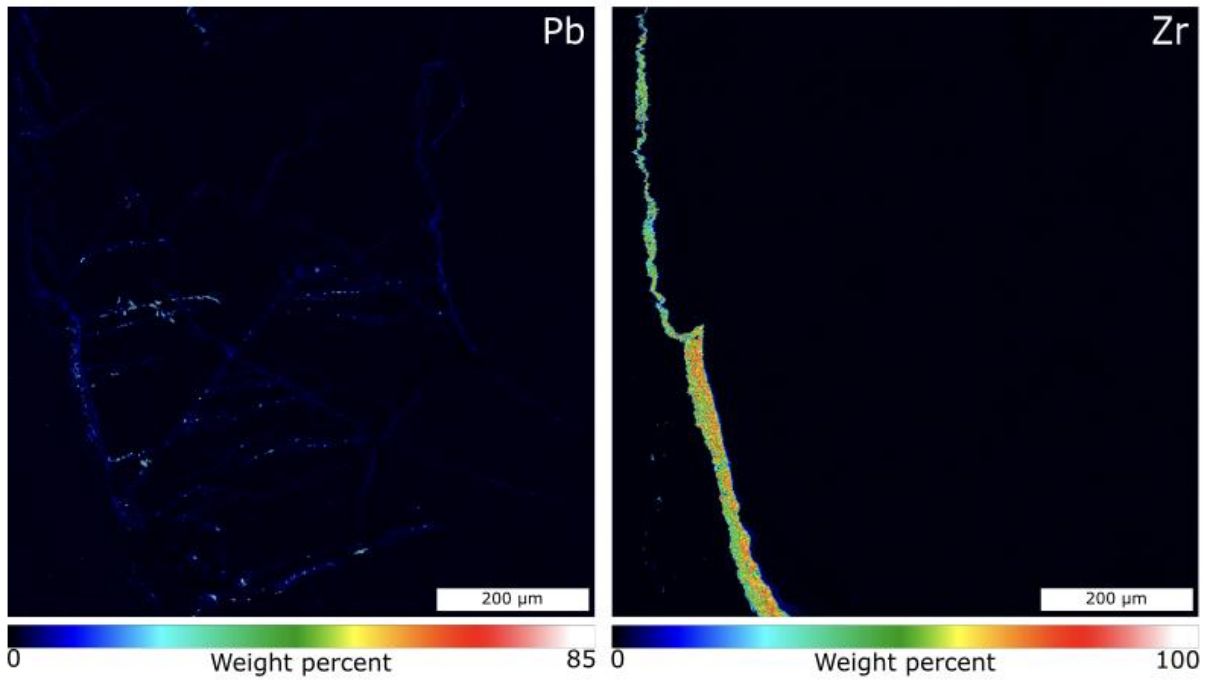
370



371

372 Figure S2. Qualitative EPMA data for relative concentrations of Pb and Ca.

373

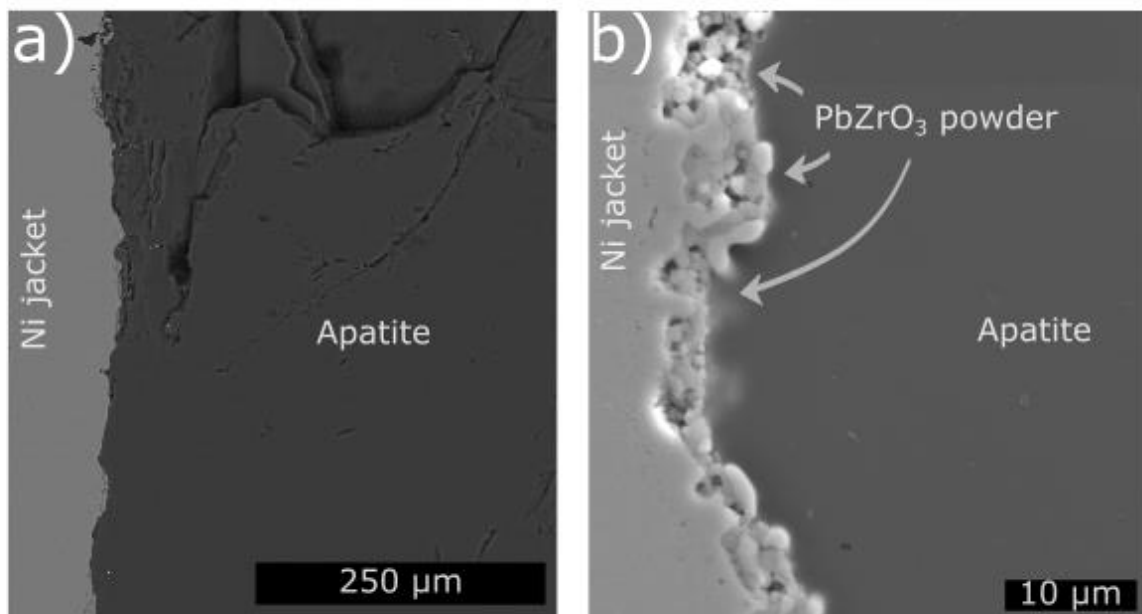


374

375 Figure S3. Quantitative sample-scale EPMA data for the dynamic diffusion experiment.

376 *Results from null experiment*

377 The null experiment consisted of bringing a sample coated in  $\text{PbZrO}_3$  to target conditions for 5 hours without  
 378 deformation. This sample was sectioned, polished, and imaged with BSE as described above. The resulting  
 379 BSE image (Fig. S4) exhibits no apparent heterogeneity, which is comparable to the static-diffusion  
 380 experiment after torsion (Fig. 1C) and in contrast to the dynamic-diffusion experiment (Fig. 1D).



381

382 Figure S4A and B. BSE images of the null experiment.

383 **Supplementary References**

384 Blavette, D., Cadel, E., Fraczkiwicz, A., and Menand, A., 1999, Three-dimensional atomic-scale imaging of  
385 impurity segregation to line defects: *Science*, v. 286, p. 2317–2319.

386 Cadel, E., Fraczkiwicz, A., and Blavette, D., 2003, Atomic Scale Investigation of Impurity Segregation to  
387 Crystal Defects: *Annual review of materials research*, v. 33, p. 215–231.

388 Fayon, A.K. and Hansen, L.N., 2018. Rheology of the rheologically insignificant mineral apatite. In  
389 *16th International Conference on Thermochemistry*.

390 Frost, H.J. and Ashby, M.F., 1982. Deformation-mechanism maps: The plasticity and creep of  
391 metals and ceramics(Book). Oxford, Pergamon Press, 1982, 175 p.

392 Paterson, M.S., and Olgaard, D.L., 2000, Rock deformation tests to large shear strains in  
393 torsion: *Journal of Structural Geology*, v. 22, p. 1341–1358.

394

395

396